# Phase stability and thermodynamic database validation in a set of non-equiatomic Al-Co-Cr-Fe-Nb-Ni high-entropy alloys

Martin Detrois[1,2], Stoichko Antonov[3,4,*], Sammy Tin[4]

[1] National Energy Technology Laboratory, 1450 Queen Ave SW, Albany, OR 97321, USA
[2] AECOM, P.O. Box 1959, Albany, OR 97321, USA
[3] State Key Laboratory for Advanced Metals and Materials, University of Science and Technology Beijing, Beijing 100083, China
[4] Illinois Institute of Technology, 10 W. 32nd Street, Chicago, IL 60616, USA

* Corresponding author. *E-mail address:* santonov@iit.edu

**Abstract**

A series of six high-entropy alloys in non-equiatomic proportions were produced to study the phase stability across a range of the compositions within the Al-Co-Cr-Fe-Nb-Ni system. Phase identification was performed using SEM, TEM, and XRD and computational tools were employed for comparison to the experimental findings. Complex microstructures were obtained following exposure at 900°C with precipitation of Laves, NiAl, γ′ and δ phases. Both primary and secondary Laves were identified and found to become more stable with increasing Fe and Nb content. Additions of Nb promoted the formation of thin plate-like δ phase at the expense of the secondary Laves. The NiAl phase was observed to precipitate in the alloys with high Fe content, above the γ′ solvus temperature. Overall, the thermodynamic predictions using Thermo-Calc with the TCNi8 database were accurate with respect to identifying the phase composition, while TTNi8 provided good phase stability results. However, significant differences were observed with respect to the solvus temperatures of the precipitate phases.

**Keywords:** A. high-entropy alloys; B. alloy design, phase stability; D. microstructure; E. phase stability, prediction; G. aerospace structures

## 1. Introduction

The pressure for increased efficiency requirements in power generation applications such as advanced gas turbines in air-based applications or steam turbines in power plants has created a

need for novel high temperature materials [1]. Oftentimes, one of the critical design considerations is increasing the operating temperature, which is typically limited by the temperature capability of the materials employed. As such, materials with enhanced thermo-mechanical properties are in constant demand. To date, Ni-based superalloys, and more recently γ′ strengthened Co-based superalloys [2], are essential for fabrication of components that are to be subjected to high stresses at elevated temperatures [3]. The microstructure of these alloys consists primarily of γ′ ($Ni_3Al$) precipitates, with an ordered $L1_2$ crystal structure, coherently embedded within a γ matrix, with a face-centered cubic (FCC) crystal structure. These precipitates are subject to anomalous strengthening at high temperatures, allowing the alloys to be used up to ~80% of their melting point [4]. In the design of superalloys, elemental additions are typically added to the base, or principal element (Ni), with aim of improving specific properties. Some will preferentially partition to the matrix, which confers solid-solution strengthening (for example, Cr, Co, Mo, W), while others (Al, Ti, Ta, Nb) enhance the precipitation of the γ′ phase, and improve intrinsic properties such as precipitate strength, anti-phase boundary energy, and stacking fault energy [5–10]. Additionally, trace elements (C, B, Hf, Zr) permit the precipitation of borides and carbides, that are often beneficial to the control of the grain structure in wrought alloys as well as improving grain boundary cohesion and reducing grain boundary diffusion thereby resulting in improved creep properties [10–15].

In recent years, high-entropy alloys (HEAs) have been widely investigated for their potential at replacing current commercial alloys [16]. This class of alloys relies on several "principal" elements as opposed to a singular one in the case of Ni-based superalloys or steels (Fe-based). By having at least five principal elements with concentrations between 5 and 35 at.%, HEAs have high entropies of mixing, typically characterized by the configurational entropy term [17], and high lattice strains arising from elements of different atomic radii [18]. Although, a single solid-solution phase alloy is attractive due to the superior ductility and stability, such alloys are often limited in creep, due to the low strength and lack of barriers to dislocation motion [19]. Conversely, formation of coherent, intermetallic precipitate phases, while maintaining a medium to high entropy of the matrix, may potentially combine the desirable properties of single phase HEAs with a potent degree of precipitation strengthening. This was shown by He et al., who calculated that the strengthening increment due to precipitation strengthening is most potent and that select phases can significantly increase the strength of the alloy while preserving its ductility [20,21]. Over the last few years, many researchers have

conducted investigations aimed at understanding the secondary precipitate phase formation in a number of well-established HEA systems [22,23]. The precipitation of γ′ in the existing alloys has primarily been achieved through the use of Ti and Al [20,24,25]. He et al. showed that small amounts of Al and Ti to the equiatomic Ni-Cr-Fe-Co system can be used to promote $L1_2$ nano-sized γ′ precipitate formation [20,21]. These nano-spheres had a high concentration of Fe, Cr and Co, not typical of the γ′ phase composition in traditional superalloys. Interestingly, independent Al and Ti additions did not promote γ′ phase formation, and thermodynamic predictions showed that the $L1_2$ formation occurs as a result of a synergistic effect between Al and Ti [16,24,26,27]. Finally, Nb additions in the NiCoCrFe and NiCoCrFeAl equimolar and non-equimolar systems did not report γ′ formation [28–30], meanwhile, computational studies on the Ni-Cr-Fe-Nb system show that $Ni_3Fe$ is the only stable $L1_2$ phase, albeit at lower temperatures, >790K [31]. However, our previous study has also confirmed that Nb also exhibits a synergistic effect with Al in promoting a stable γ′ phase for specific compositional ranges [32].

In this investigation, the Co-Cr-Fe-Ni system was investigated in order to study the influence of Al and Nb additions on the precipitate phase formation and stability. Nb was chosen instead of Ti as it is known to promote the formation of γ′ precipitates, while also partitioning to the matrix, providing additional levels of solid-solution strengthening [33]. Although this novel alloy system appears promising, a variety of undesirable phases have been shown to form [32]. Thus, there is a need to pursue experimental investigations which document and characterize the resulting phase formation/stability in the system and establish the solubility limits. In this study, three Ni-rich and three Co-rich alloys were investigated at temperatures at and above targeted operating conditions for high-temperature applications. Furthermore, the accuracy of the thermodynamic predictions is assessed.

## 2. Procedure

A set of non-equiatomic Al-Co-Cr-Fe-Nb-Ni high-entropy alloys, with varying levels of Al, Fe and Nb, was explored. The compositions of the alloys are listed in Table 1 using the following nomenclature: $\alpha$Fe-$\beta$Al-$\gamma$Nb where $\alpha$, $\beta$ and $\gamma$ are the concentrations of Fe, Al and Nb in atomic percent, respectively. All the alloys were prepared from elemental metals with purity of 99.95% or greater to a target weight of 100 g. The stock material was melted with a non-consumable tungsten electrode in a MRF ABJ-900 arc melter under argon partial pressure. The

arc melter chamber was purged to a pressure of $10^{-3}$ mbar and backfilled with high purity argon (99.998%) prior to melting each alloy. The process was repeated four times to ensure cleanliness of the arc melt ingots. Subsequently, each ingot was melted and remelted up to six times to convectively mix and uniformly distribute the elemental additions throughout the structure. A 100 g Ti getter was melted in between each step to further reduce gaseous impurities during melting. Following melting, the ingots were homogenized under vacuum in a tube furnace using a two-step heat treatment consisting of a 1°C/h ramp from 1150°C to 1200°C and a soaking time of 50 h at 1200°C. Finally, four different heat treatments were investigated and consisted of 100 h at 800°C, 900°C, 1000°C, or 1100°C followed by air cooling.

Metallographic characterization was performed at each step of the fabrication process following sample preparation with a final polish using 0.6 μm colloidal silica. Observation of the cast and homogenized microstructures was performed using a JEOL JSM 5900-LV scanning electron microscope (SEM) in backscatter electron (BE) mode. Observation of the aged microstructures was conducted using a FEI Inspect F SEM in BE mode with preliminary phase identification performed using an Oxford Instruments X-Max energy dispersive spectrometer (EDS) connected to the SEM. Quantification of precipitate size and aspect ratio was performed using the image analysis software ImageJ [34] with the script detailed in Ref. [35].

Additional phase identification was performed using X-ray diffraction (XRD) analysis on specimens ground to 2000 grit SiC using a Bruker D8 Advance diffractometer with a Co K-α tube, at an energy of 35 V and 40 A, for a 2θ range of 20º to 120º and a step size of 0.02º with a 4 s dwell time. A spinning stage was used in order to minimize preferred orientation. Finally, Rietveld analysis was performed using GSAS II with crystallographic information files built from EDS data with VESTA [36,37].

To further identify the secondary phases that formed in the alloys during the long-term thermal exposure, thin foils for transmission electron microscopy (TEM) observation were prepared by punching 3 mm diameter disks from the bulk material and manually grinding them to 50 μm. Subsequently, the discs were subjected to twin-jet thinning in a solution of 7% Perchloric acid and 93% ethanol at -40°C and 40 V. A FEI Tecnai F30 transmission electron microscope operated at 300 kV was used for observation, selective area diffraction (SAD), and energy dispersive spectroscopy (EDS). SAD patterns were indexed with the aid of diffraction patterns simulated by SingleCrystal.

Thermodynamic simulations were performed using Thermo-Calc (v2017b). The two most employed databases for Ni-based alloys, TCNi8 and TTNi8, were considered in this investigation due to the relatively high Ni content of the present alloys. It should be noted that additional simulations were performed using the database TCHEA2 which resulted in very similar results than those from TCNi8 and therefore the results were omitted in this manuscript. The temperature range for the simulation are reported from 600°C to past the liquidus temperature to focus on the targeted operating conditions and solubility limits of the various phases.

**Table 1.** Nominal compositions of the HEA alloys (at. %).

| Alloy | Al | Co | Cr | Fe | Nb | Ni |
|---|---|---|---|---|---|---|
| 9Fe-8Al-4Nb | 8 | 30 | 18 | 9 | 4 | 31 |
| 9Fe-6Al-6Nb | 6 | 30 | 18 | 9 | 6 | 31 |
| 9Fe-4Al-8Nb | 4 | 30 | 18 | 9 | 8 | 31 |
| 18Fe-8Al-4Nb | 8 | 30 | 18 | 18 | 4 | 22 |
| 18Fe-6Al-6Nb | 6 | 30 | 18 | 18 | 6 | 22 |
| 18Fe-4Al-8Nb | 4 | 30 | 18 | 18 | 8 | 22 |

## 3. Results

The conventional parameters used to classify HEAs were calculated and the results are listed in Table 2. The enthalpy of mixing ($\Delta H_{mix}$), the configurational entropy of mixing ($\Delta S_{mix}$) as a function of the gas constant $R$, the valence electron concentration (VEC), and the atomic size difference (δ) were determined using the equations available in Refs. [18,38]. The results for the configurational entropy of mixing classify these alloys as high-entropy, regardless whether they form a single phase or intermetallic phases, as the ($\Delta S_{mix}$) value is ~1.6R [17]. The VEC was calculated at approximately 8 which is indicative of a preferred FCC crystal structure [23]. Doubling the Fe content resulted in higher entropy of mixing and lower enthalpy of mixing with the entropy of mixing of all the alloys greater than 1.58$R$. The information in Table 2 is provided for reference to the reader to compare this set of alloys to other HEAs. It is important to note that even though the overall configurational entropy of the alloys is high, the formation of precipitate phases may result in a reduction of entropy of the matrix due to the partitioning of certain elemental species to the newly formed precipitate phases.

**Table 2.** Calculated thermodynamic properties of the HEA alloys.

| Alloy | $\Delta H_{mix}$ (kJmol$^{-1}$) | $\Delta S_{mix}$ (JK$^{-1}$mol$^{-1}$) | $\Delta S_{mix}$ | VEC | $\delta$ |
|---|---|---|---|---|---|
| 9Fe-8Al-4Nb | -11.1 | 13.14 | 1.58*R* | 8.04 | 4.69 |
| 9Fe-6Al-6Nb | -11.4 | 13.20 | 1.59*R* | 8.08 | 4.68 |
| 9Fe-4Al-8Nb | -11.7 | 13.14 | 1.58*R* | 8.12 | 4.67 |
| 18Fe-8Al-4Nb | -10.4 | 13.66 | 1.64*R* | 7.86 | 4.71 |
| 18Fe-6Al-6Nb | -10.7 | 13.71 | 1.65*R* | 7.90 | 4.70 |
| 18Fe-4Al-8Nb | -11.0 | 13.66 | 1.64*R* | 7.94 | 4.69 |

The Thermo-Calc results for alloy 9Fe-6Al-6Nb are represented in Fig. 1 and the crystallographic information of the phases predicted in the phase diagrams and commonly encountered in Ni-based superalloys are summarized in Table 3 for reference. Both databases predicted the formation of Laves, δ and σ phase in addition to the γ (Ni) matrix. The σ phase will be ignored in the remaining of this investigation as it is known to form only after extended time at temperature [4]. Although a fourth precipitate phase was predicted to form, the databases were in disagreement; TCNi8, Fig. 1(a), predicted formation of NiAl while TTNi8 predicted the formation of η phase, Fig. 1(b). Finally, if η was removed from the computation using TTNi8, formation of γ′ precipitates was predicted instead, Fig. 1(c).

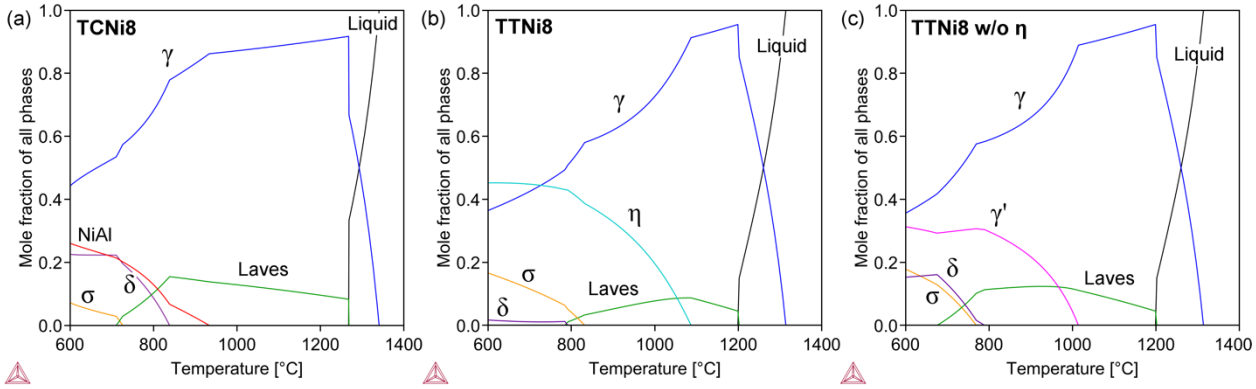


**Fig. 1.** Thermo-Calc phase predictions for the alloy 9Fe-6Al-6Nb using (a) the TCNi8, (b) the TTNi8 and (c) the TTNi8 (with η removed) databases.

**Table 3.** Description of the typical phases encountered in Ni-based superalloys.

| Phase | Typical Composition | Crystal Structure | Space Group | Pearson Symbol | Lattice Parameters |
|---|---|---|---|---|---|
| **γ** | (Ni,Co,Cr,Al,Mo,W,Nb) | FCC | $Fm\bar{3}m$ | cF4 | a ≥ 0.352 |
| **γ'** | $(Ni,Co)_3(Al,Nb,Ti,Ta)$ | Ordered FCC | $Pm\bar{3}m$ | cP4 | a ≥ 0.356 |
| **η** | $Ni_3Ti$ | HCP | $P6_3/mmc$ | hP16 | a = 0.509-0.512, c = 0.831-0.835 |
| **δ** | $Ni_3Nb$ | Orthorhombic | Pmmm | oP8 | a = 0.510-0.512, b = 0.521-426, c = 0.452-457 |
| **σ** | (Cr,Mo)x(Ni,Co)y | Tetragonal | $P4_2/mnm$ | tP30 | a = 0.880-0.922, c = 0.450-0.482 |
| **NiAl** | (Ni,Co)(Al,Nb) | Ordered BCC | $Pm\bar{3}m$ | cP2 | a = 0.286-0.288 |
| **Laves-C14** | $(Fe,Cr,Co,Ni)_2Nb$ | Hexagonal | $P6_3/mmc$ | hP12 | a = 0.475-0.495, c = 0.770-0.815 |
| **MC** | (Ti,Zr,Hf,V,Nb,Ta)C | FCC | Fm3m | cF8 | a = 0.430-0.470 |

The Laves phase was predicted to be stable up to the incipient melting temperature for all of the alloys at the exception of alloy 9Fe-8Al-4Nb with TTNi8. The phase fraction was found to increase with increasing Nb and/or Fe content. According to the Thermo-Calc phase composition predictions listed in Table 4, the Laves phase is rich in Co and Nb with partitioning of Cr, Fe and Ni. The solvus temperatures of the other precipitate phases were plotted as a function of the Al and Nb content in Fig. 2 for a more visible comparison of the predictions from the two databases. Note that predictions below 600°C were omitted as those temperatures are beyond the scope of this investigation. Intuitively, the predicted solvus temperature of the NiAl phase, as well as its fraction (not represented), was predicted to decrease with decreasing Al content. Interestingly, both solvus temperature and fraction were found to increase when the Fe content was doubled in the 18 at.% Fe alloys. While the TCNi8 database predicts stability of the NiAl phase for all of the alloys, the 9 at.% Fe alloys with 6Al-6Nb and 4Al-8Nb are not predicted to precipitate NiAl from TTNi8. From Table 4, the NiAl phase exhibits strong partitioning of Co and less significant concentrations of Cr and Fe from TCNi8 while TTNi8 predicts partitioning of Co and Nb.

The formation of δ phase is predicted from both databases with increasing solvus temperature and fraction with increasing Nb content. Its composition, listed in Table 4, is in agreement with the accepted composition range of $Ni_3Nb$ with additional partitioning of Co. It was observed on phase diagrams that the δ phase stability competes with the Laves phase which can be observed in Fig. 1. Increasing the Fe content was found to decrease the δ solvus

temperature and fraction according to the TCNi8 predictions. TTNi8 only predicted formation of the δ phase in the 9Fe-6Al-6Nb and 9Fe-4Al-8Nb alloys.

While TTNi8 did not predict the formation of δ phase for all of the alloys, it predicted the formation of the ordered η phase with $(Ni,Co)_6AlNb$ composition, Table 4. Finally, the γ′ phase ($Ni_3Al$) was predicted to form in the alloy with the lowest Fe and Nb content and highest Al content 9Fe-8Al-4Nb according to the TTNi8 database. If the η phase was removed from the computation, the γ′ phase is predicted in all of the alloys. TCNi8 did not report formation of the γ′ phase in the temperature range investigated.

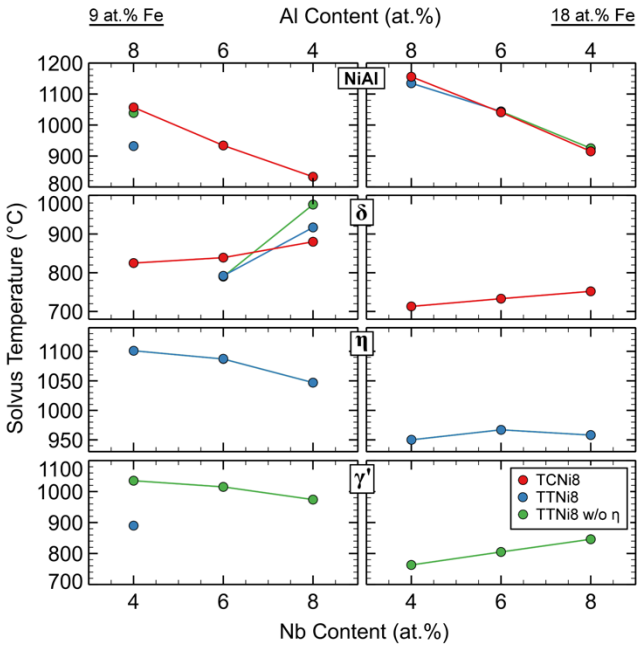


**Fig. 2.** Solvus temperatures of the NiAl, δ, η and γ′ phases from Thermo-Calc using the TCNi8, TTNi8 and TTNi8 without η phase in the set of HEAs investigated.

**Table 4.** Phase compositions from the Thermo-Calc predictions in the alloy 18Fe-6Al-6Nb for Laves and NiAl and 9Fe-4Al-8Nb for δ and η (at. %).

| Phase | Database | Al | Co | Cr | Fe | Nb | Ni |
|---|---|---|---|---|---|---|---|
| Laves (900°C) | TCNi8 | 2.1 | 34.7 | 11.5 | 13.1 | 30.4 | 8.2 |
| | TTNi8 | - | 25.6 | 13.7 | 15.5 | 26.4 | 18.8 |
| NiAl (900°C) | TCNi8 | 25.7 | 23.5 | 7.3 | 14.0 | 0.6 | 29.0 |
| | TTNi8 | 35.0 | 7.4 | 1.0 | 2.2 | 9.8 | 44.6 |
| δ (800°C) | TCNi8 | 0.1 | 13.0 | 1.0 | 1.1 | 24.8 | 60.0 |
| | TTNi8 | 3.4 | 15.0 | 1.2 | 1.0 | 21.6 | 57.8 |
| η (900°C) | TTNi8 | 11.9 | 29.9 | 0.1 | 1.0 | 13.0 | 44.1 |

Micrographs of the as-cast and homogenized conditions are represented in Fig. 3 for the two extreme compositions. Increasing the Nb and Fe content resulted in an increase in the amount of eutectic phase present in the as-cast condition, Fig. 3(a,c). Following homogenization, only primary Nb-carbides (NbC) remained in the microstructure of the alloy 9Fe-8Al-4Nb, Fig. 3(b), while all the others contained a remnant phase observed in Fig. 3(d). The NbC are desirable and formed from the carbon naturally present in some of the stock material as well as from the melting process. The amount of remnant phase was found to increase with the Nb and Fe content with a more pronounced increase associated with Nb. Preliminary EDS analysis revealed the remaining phase to be primary Laves precipitates which was confirmed in an earlier investigation [32].

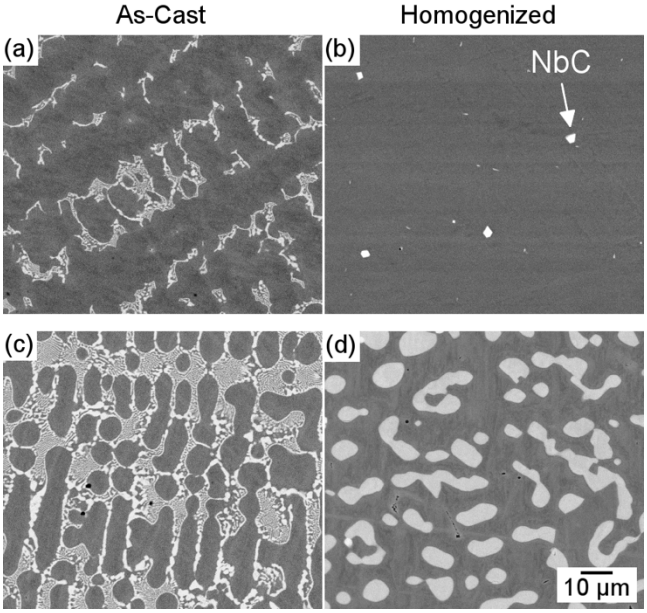


**Fig. 3.** Microstructure of alloy 9Fe-8Al-4Nb in (a) the as-cast condition and (b) following homogenization and alloy 18Fe-4Al-8Nb in (c) the as-cast condition and (d) following homogenization.

The microstructures of the alloys following 100 h at 800°C are shown in Fig. 4. The primary Laves phases observed following homogenization are the largest globular bright gray precipitates in alloys 9Fe-6Al-6Nb, Fig. 4(b), and 9Fe-4Al-8Nb, Fig. 4(c), as well as the three alloys containing 18 at.% Fe, Fig. 4(d-f). A second phase of similar brightness formed in all of

the 18 at.% Fe specimens in the form of sub-micron sized plates. Image analysis of the microstructure of alloy 18Fe-6Al-6Nb, Fig. 4(e), revealed a maximum Feret size of 0.5 ± 0.2 μm and a 3.7 ± 1.5 aspect ratio, averaged over 348 precipitates. Also in the 18 at.% Fe alloys, another sub-micron sized plate-like phase was observed in black. The phase was located around the Laves at the γ/Laves interface and along the sub-micron brighter plate-like phase in alloy 18Fe-8Al-4Nb, Fig. 4(d). With decreasing Al and increasing Nb content, only the precipitates at the γ/Laves interface remained in alloy 18Fe-6Al-6Nb, Fig. 4(e), and none were observed in alloy 18Fe-4Al-8Nb, Fig. 4(f). Instead a thin nano-sized needle like phase can be observed. This needle like phase was also observed in alloy 9Fe-6Al-6Nb, Fig. 4(b), on and around the Laves precipitates and also in the matrix of alloy 9Fe-4Al-8Nb, Fig. 4(c). Finally, nano-sized precipitates were observed in the higher magnification insets of the 9 at.% Fe alloys with average diameters below 100 nm.

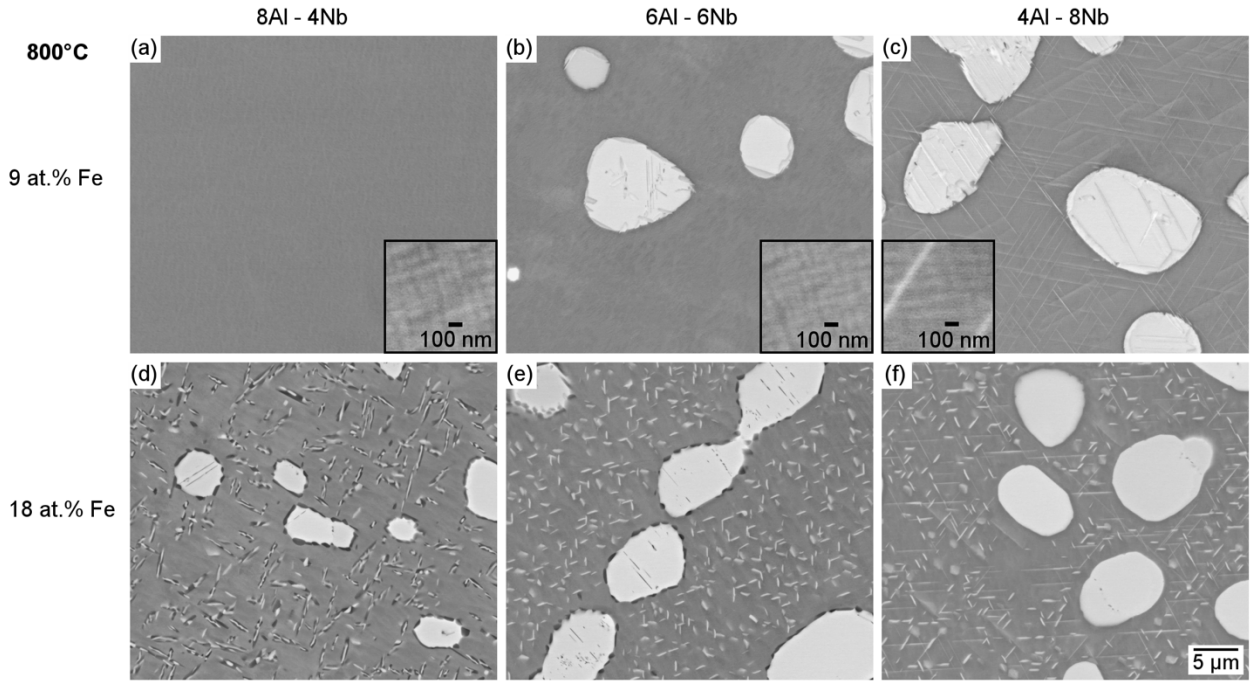


**Fig. 4.** Microstructure of the alloys following 100 h at 800°C with (a,b,c) 9Fe, (d,e,f) 18Fe, (a,d) 8Al-4Nb, (b,e) 6Al-6Nb and (c,f) 4Al-8Nb.

Following heat treatment at 900°C for 100h, Fig. 5, the sub-micron bright plates remained in the 18 at.% Fe alloys and become more plentiful in the alloy with higher Nb

concentration, 18Fe-4Al-8Nb in Fig. 5(f), while the needle phase dissolved. Those precipitates have a maximum Feret of 0.80 ± 0.25 μm and 3.1 ± 0.9, respectively in alloy 18Fe-4Al-8Nb, Fig. 5(f), based on measurements of over 497 precipitates. The sub-micron plates were also present in two of the 9 at.% Fe alloys, particularly in the 9Fe-8Al-4Nb alloy, Fig. 5(a), with a maximum Feret of 2.6 ± 1.2 μm and aspect ratio of 3.8 ± 1.3 calculated over 164 precipitates. They became less prevalent with increasing Nb (or decreasing Al) content in 9Fe-6Al-6Nb, Fig. 5(b), and were not observed in 9Fe-4Al-8Nb, Fig. 5(c). Instead, a phase with Widmanstätten morphology further precipitated forming an intricate structure of thin elongated needles in those alloys. Interestingly, a similar, although wider, thin plate like phase formed around the Laves precipitates of alloy 9Fe-4Al-8Nb, Fig. 5(c), following the same orientations as the thin elongated needles structure. Finally, the fraction of the black plate-like phase in the 18 at.% Fe alloys was found to decrease with decreasing Al (increasing Nb) content. The phase was observed to reside along the large Laves and small bright plates in alloy 18Fe-8Al-4Nb, Fig. 5(d), and only along the large Laves in alloy 18Fe-6Al-6Nb, Fig. 5(e), similar to the 800°C condition. The precipitates maximum Feret and aspect ratio were calculated at 0.9 ± 0.4 μm and 2.4 ± 1.1, respectively, over 132 precipitates in alloy 18Fe-6Al-6Nb, Fig. 5(e). After this 900°C heat treatment condition, only alloys 9Fe-8Al-4Nb and 9Fe-6Al-6Nb, Fig. 5(a,b), contained the nano-sized precipitates observed in Fig. 4. This phase was not present in the high-Nb alloy.

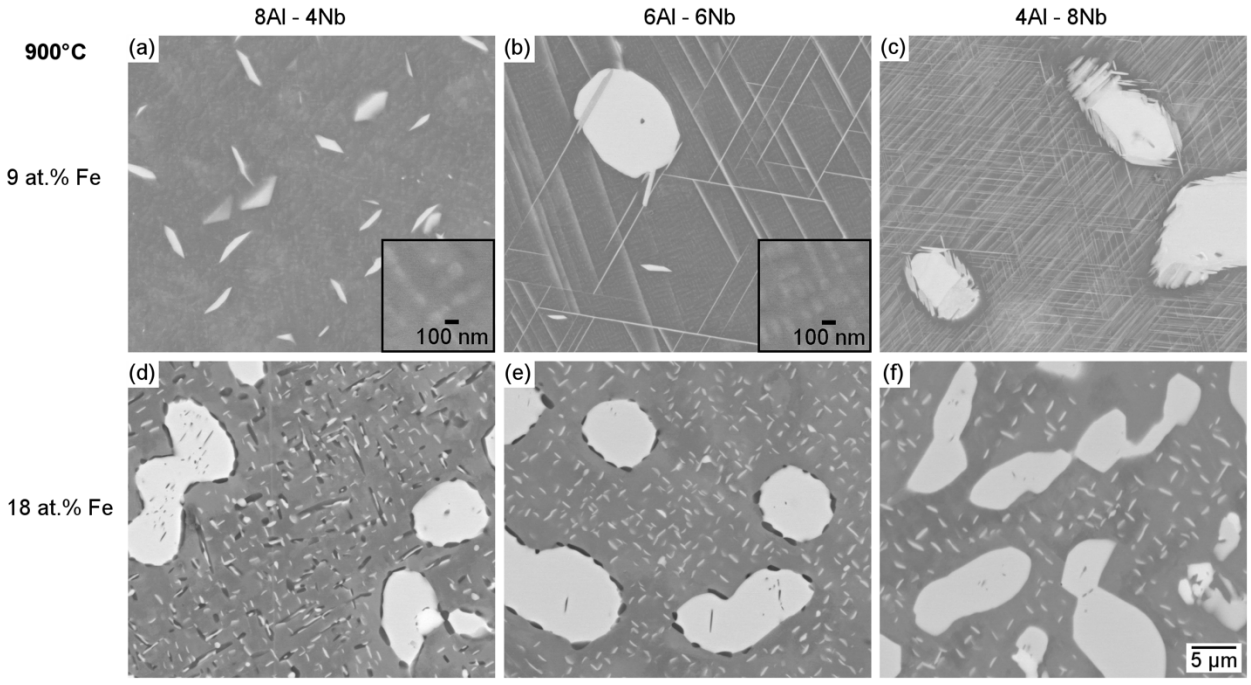

**Fig. 5.** Microstructure of the alloys following 100 h at 900°C with (a,b,c) 9Fe, (d,e,f) 18Fe, (a,d) 8Al-4Nb, (b,e) 6Al-6Nb and (c,f) 4Al-8Nb.

Following heat treatment at 1000°C for 100 h, as shown in Fig. 6, the thin needle-like phase dissolved while the small bright plates are still present. The small plates grew when compared to the 900°C heat treatment in alloy 9Fe-4Al-8Nb, Fig. 6(c), (maximum Feret of 9.3 ± 3.5 µm and aspect ratio of 5.3 ± 1.5 over 226 precipitates) while they were present in greater number density in the alloys that formed the thin needle-like phase at 900°C: 9Fe-6Al-6Nb and 9Fe-4Al-8Nb, Fig. 6(b,c). A visibly lower number density of the plates was observed in the alloys containing 18 at.% Fe. Additionally, fewer of the black sub-micron plates were present in alloy 18Fe-8Al-4Nb, Fig. 6(d), and those were completely dissolved in alloy 18Fe-6Al-6Nb, Fig. 6(e). Finally, heat treatment at 1100°C resulted in the complete dissolution of all the precipitate phases at the exception of the primary Laves and large plates in alloy 9Fe-8Al-4Nb, Fig. 6(a), that continued to grow.

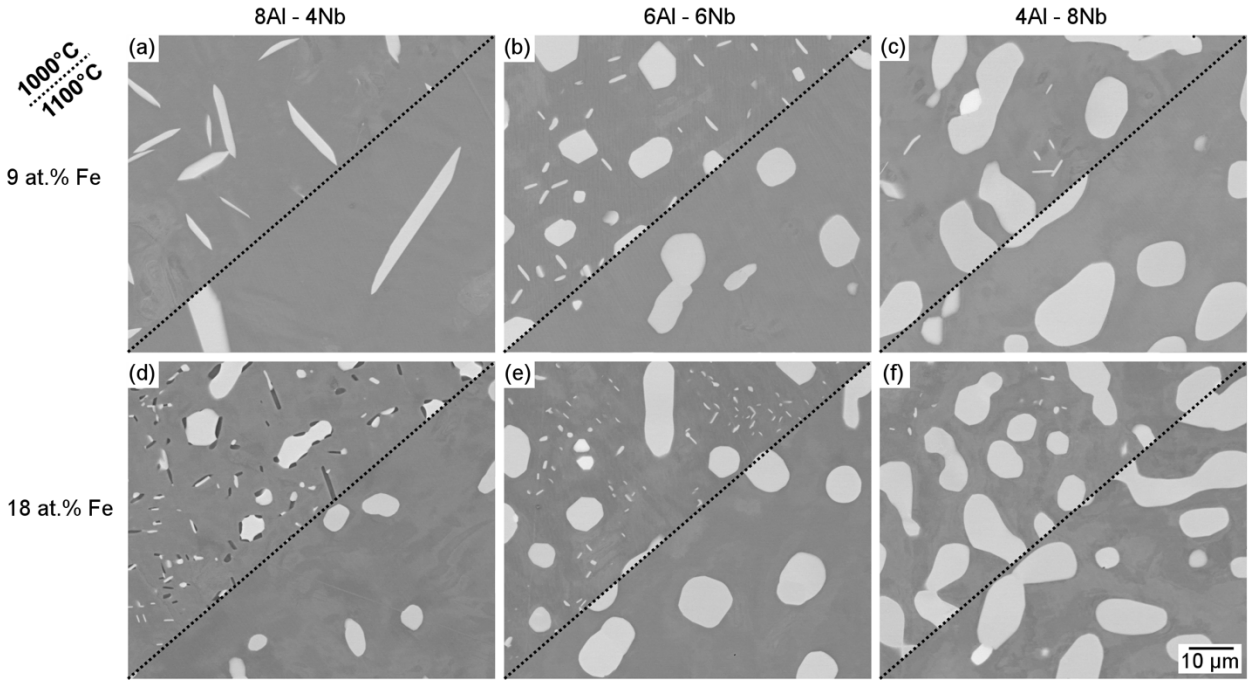


**Fig. 6.** Microstructure of the alloys following 100 h at 1000°C and 1100°C with (a,b,c) 9Fe, (d,e,f) 18Fe, (a,d) 8Al-4Nb, (b,e) 6Al-6Nb and (c,f) 4Al-8Nb.

The XRD patterns for all of the alloys heat treated for 100 h at 900°C are represented in Fig. 7. The results revealed a predominant FCC crystal structure in all of the alloys. In addition, C14-Laves was found in all the 18 at.% Fe HEAs and alloys 9Fe-6Al-6Nb and 9Fe-4Al-8Nb. Small peaks representative of a B2 crystal structure were detected in the alloy 18Fe-8Al-4Nb. Finally, evidence of a phase of $D0_a$ crystal structure was found in the alloys 9Fe-6Al-6Nb and 9Fe-4Al-8Nb. More information about the phases can be found in Table 3.

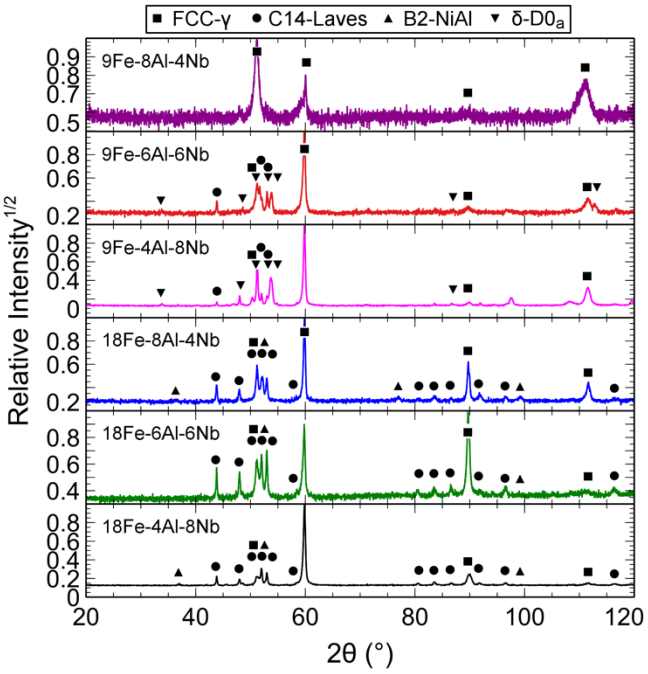


**Fig. 7.** XRD patterns for the alloys after heat treatment of 100 h at 900°C.

Results from TEM analysis on the 18Fe-6Al-6Nb alloy are shown in Fig. 8 with a magnified region of the SEM image of Fig. 5(e) shown in Fig. 8(b). The primary Laves were confirmed with a hexagonal C14 crystal structure. The composition of the primary Laves phase is listed in Table 5 for this alloy and consisted of 32 at.% Co, 31 at.% Nb, 11 at.% Cr, 13 at.% Fe, 12 at.% Ni and minor partitioning of Al. The sub-micron sized bright plates observed on the SEM images were identify in Fig. 8(a) also as C14-Laves. Their composition is very similar to that of the primary Laves precipitates, Table 5. Finally, the black plate-like precipitates observed on the SEM images were identified, in bright gray in Fig. 8(a), as NiAl phase with an ordered body-centered cubic (BCC) B2 crystal structure. From Table 5, the NiAl phase was also rich in Co and Fe. The γ matrix phase was also characterized to confirm the FCC crystal structure, and

311 to confirm the absence of any nano-scale $L1_2$ precipitates. It should be noted that a similar
312 analysis was performed for the 18Fe-4Al-8Nb and 18Fe-8Al-4Nb alloys, however, only the
313 results for 18Fe-6Al-6Nb are shown, as this alloy exhibits all of the phases.

314

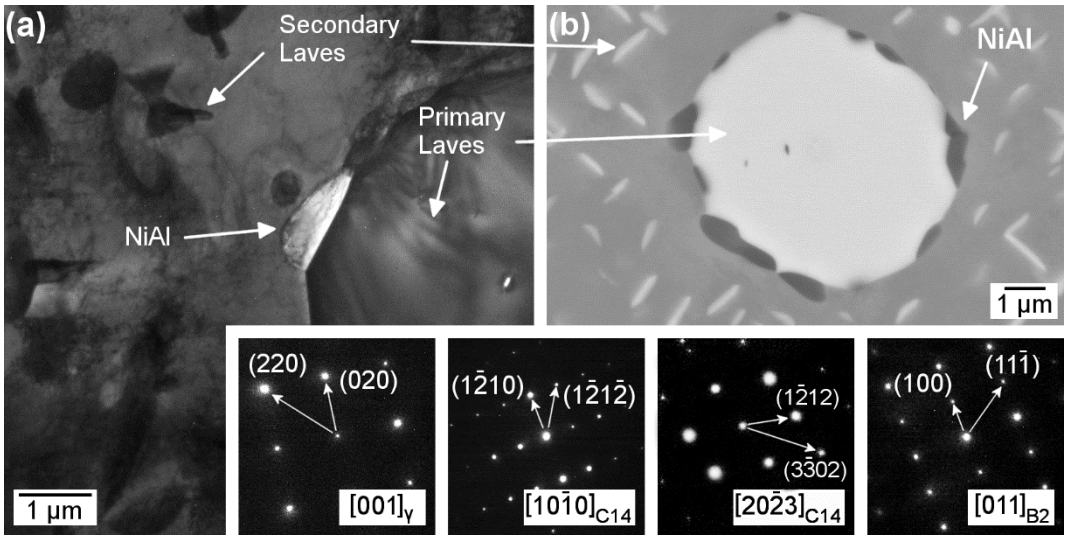


315

316 **Fig. 8.** (a) TEM micrograph showing the matrix, primary and secondary Laves, and NiAl phases
317 with the corresponding SAD patterns in the $[001]_{\gamma}$, $[10\bar{1}0]_{C14}$, $[20\bar{2}3]_{C14}$, and $[011]_{B2}$ zone axes,
318 respectively, and (b) a corresponding BE image in alloy 18Fe-6Al-6Nb after 100 h at 900°C

319

320 Results from TEM analysis on the 9Fe-4Al-8Nb alloy are shown in Fig. 9 with a
321 magnified region of the SEM image of Fig. 5(c) shown in Fig. 9(b). The γ matrix was found to
322 be of FCC crystal structure, with absence of any nano-scale $L1_2$ precipitates, and the large
323 primary Laves phase was confirmed with a C14 crystal structure. The needle-like phase within
324 the matrix observed in Fig. 5(c) can be observed in black in Fig. 9(a). The phase was identified
325 as δ phase with a $D0_a$ crystal structure, with a typical Widmanstätten morphology [30]. However,
326 the limited size of the precipitate made it difficult to obtain quantitative TEM-EDS data without
327 sampling the surrounding matrix. The larger plates along the primary Laves precipitate, in bright
328 gray in Fig. 9(a), were also determined to be δ phase with $D0_a$ crystal structure and TEM-EDS
329 spectra were obtained from these precipitates. Aside the common $Ni_3Nb$ composition, this δ
330 phase was found to be rich in Co, Table 5. Based on the SEM micrographs, it could be judged
331 that the needle-like phase in the matrix would have a similar composition to those along the
332 Laves phase, purely based on the contrast of the BE image. It is also worth noting that the δ

phase adjacent to the Laves precipitates has the same growth orientation direction as the δ phase within the matrix, further supporting the argument that this is the same phase. The needle-like phase in the 9Fe-6Al-6Nb alloy observed in Fig. 5(b) was also identified as δ phase with a $D0_a$ crystal structure; not shown here.

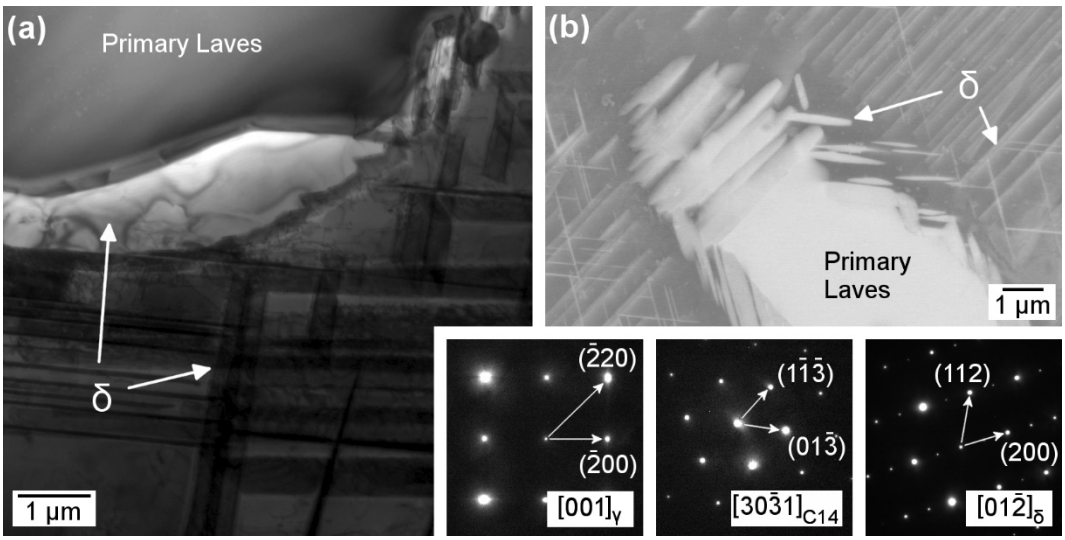


**Fig. 9.** (a) TEM micrograph showing the matrix, primary Laves, and δ phases with the corresponding SAD patterns in the $[001]_\gamma$, $[30\bar{3}1]_{C14}$, and $[01\bar{2}]_\delta$ zone axes, respectively, and (b) a corresponding BE image in alloy 9Fe-4Al-8Nb after 100 h at 900°C.

**Table 5.** Phase compositions from TEM EDS in the alloy 18Fe-6Al-6Nb for Laves and NiAl and 9Fe-4Al-8Nb for δ after 100 h at 900°C (at.%).

| Alloy | Al | Co | Cr | Fe | Nb | Ni |
|---|---|---|---|---|---|---|
| Primary Laves | 0.7 | 32.4 | 10.9 | 13.1 | 31.0 | 11.9 |
| Secondary Laves | 0.7 | 32.4 | 11.7 | 13.3 | 29.8 | 12.1 |
| NiAl | 25.0 | 19.3 | 4.2 | 11.0 | 1.8 | 39.7 |
| δ | 0.1 | 28.5 | 1.5 | 1.7 | 28.8 | 39.4 |

In addition to the primary and secondary Laves, NiAl and δ phases, nano-sized precipitates were observed in the 9 at.% Fe alloys following heat treatment at 800°C for 100 h, Fig. 4(a-c), and in alloys 9Fe-8Al-4Nb, Fig. 5(a), and 9Fe-6Al-6Nb, Fig. 5(b), following heat treatment at 900°C for 100 h. The precipitates were identified as γ′ ($Ni_3Al$) using TEM-SAD analysis, as shown in Fig. 10, revealing the ordered $L1_2$ crystal structure. The nano-sized

precipitates in the 9Fe-6Al-6Nb alloy, Figs. 4(b) and 5(b), were also confirmed as γ′ ($Ni_3Al$) using TEM-SAD; not shown here.

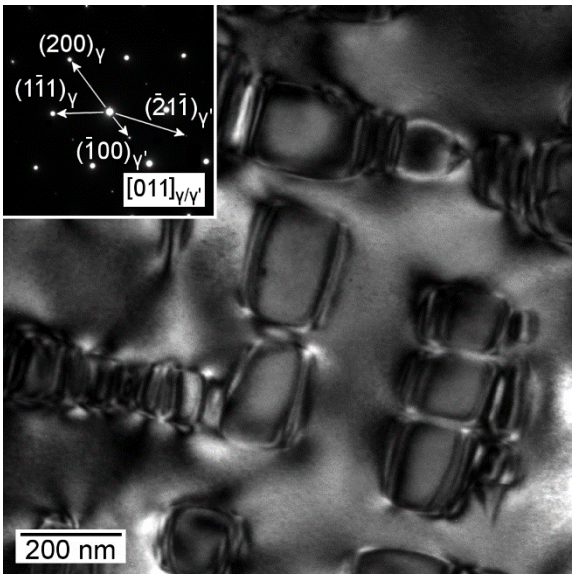


**Fig. 10.** γ′ precipitates ($Ni_3Al$) in the alloy 9Fe-8Al-4Nb, with a corresponding SAD pattern of the γ/γ' structure in the $[011]_{\gamma/\gamma'}$ zone axis, exhibiting the characteristic superlattice diffraction spots of the ordered $L1_2$ crystal structure.

## 4. Discussion

### 4.1. Homogenization

Over the six alloys investigated, only one was able to be completely solutioned during homogenization to exhibit a single phase, alloy 9Fe-8Al-4Nb. In this alloy, all the constituent eutectic phases were dissolved during the homogenization heat treatment and only Nb-carbides remained in the microstructure, Fig. 3(b). In the other alloys, the eutectic phase transformed into primary C14-Laves, Fig. 3(d) and Fig. 8. This, however, is not indicative of an incomplete homogenization process as several temperatures were investigated with various times and none resulted in the dissolution of the primary Laves prior to the onset of incipient melting. This was also observed in the Thermo-Calc phase predictions, Fig. 1, where the Laves phase is stable up to the incipient melting temperature. This was predicted for all the alloys by the TCNi8 database and all but 9Fe-8Al-4Nb using TTNi8. It should be noted that although many reports focus on the as-cast state of high entropy alloys, such a state is far from equilibrium and any potential use

at high temperature would result in a significant microstructural evolution without a proper heat treatment [39]. Furthermore, due to sluggish mobilities associated with many constituent elements in high concentrations, homogenization can be a lengthy process without the aid of CALPHAD [39,40].

Observation of the microstructures of the alloys revealed a significant increase in the fraction of primary Laves with increasing Nb and/or Fe content, Fig. 3(d). This increase was more pronounced with increasing concentrations of Nb which is consistent with previous reports on Nb additions in the NiCoCrFe system [28,32] and can be explained from the composition of the Laves phase. TEM-EDS analysis revealed Nb and Fe to be the second and third major constituents of the Laves phase at 31 and 13 at.% after Co at 32 at.%, Table 5. Therefore, decreasing the Nb and Fe content in alloy 9Fe-8Al-4Nb prevented the precipitation of primary Laves. It should be noted that no precipitation of C15 $Cr_2Nb$ or μ $(Ni,Fe)_6Nb_7$ phase was detected, even though these phases have been observed experimentally and predicted by the thermodynamic models to form in the Ni-Cr-Fe-Nb system at elevated Nb concentrations [30,31].

### 4.2. Laves phase

Heat treatment of the homogenized specimens at 900°C for 100 h produced intricate microstructures from the formation of different precipitate phases as observed in Fig. 5. The secondary Laves were present in the form of sub-micron sized plates with an average aspect ratio around 3. Both primary and secondary Laves were found to have almost identical compositions from the TEM-EDS measurements of Table 5. Thus, with no primary Laves present in alloy 9Fe-8Al-4Nb, Fig. 5(a), a greater amount and size of secondary Laves precipitates were able to form since more of the Laves constituting elements were available in solution prior to heat treatment at 900°C. Exposure at the higher temperatures of 1000°C and 1100°C resulted in the growth of the secondary Laves as they are not restricted by the large blocky primary precipitates in that alloy, Fig. 6(a). In the 18 at.% Fe alloys, the secondary Laves are more present as Fe is a strong Laves partitioning element, Fig. 5(d-f). The smaller size of the precipitates can likely be attributed to the presence of the large blocky primary Laves. Therefore, no significant change in the size of the secondary Laves was observed at the higher heat treatment temperature, Fig. 6(d-f). Finally, although Nb is a strong partitioning element to the Laves phase, increasing the Nb content resulted in a smaller number density of the secondary Laves precipitates. This can be

observed after heat treatment at 900°C, Fig. 5, and 1000°C, Fig. 6. This can also be attributed to the higher fraction of primary Laves with increasing Nb content following homogenization. Therefore, less solute is available for the formation of the secondary Laves phase during heat treatment at 900°C and 1000°C. Heat treatment at 1100°C resulted in the dissolution of the secondary Laves in the 18 at.% Fe alloys, Fig. 6(d-f), 9Fe-6Al-6Nb, Fig. 6(b), and 9Fe-8Al-4Nb, Fig. 6(c). Consequently, only the primary Laves are stable up to the incipient melting temperature, not the secondary Laves phase precipitates. Finally, no secondary Laves were observed in the 9 at.% Fe alloys following heat treatment at 800°C, Fig. 4(a-c).

From the Thermo-Calc predictions in alloy 9Fe-8Al-4Nb (not represented), TCNi8 predicts stability of the Laves phase from ~750°C to the incipient melting temperature while TTNi8 does not predict the secondary Laves to be stable unless η phase is removed at which point it becomes stable at temperatures between ~725°C to ~1050°C and is accompanied with the precipitation of the γ′ phase. It is possible that the Thermo-Calc predictions underestimated the minimum temperature in the stability range for the secondary Laves phase and 800°C may be below the minimum temperature for their formation in the 9 at.% Fe alloys.

### 4.3. Precipitate phase formation and stability

Formation and stability of the secondary Laves in the alloys containing 9 at.% Fe appears to also be affected by the other secondary phases that form. At 800°C, Fig. 4(a-c), no secondary Laves were present while the γ′ and δ precipitates were found. At 900°C, Fig. 5(a-c), both γ′ and secondary Laves precipitated in the alloy with 8Al-4Nb, Fig. 5(a), all three phases (γ′, secondary Laves and δ) were present with 6Al-6Nb, Fig. 5(b), and only the δ phase remained with 4Al-8Nb, Fig. 5(c). With compositions showing partitioning of elements common to all three phases and particularly for Laves and δ, it is evident that their stability is influenced by one another, Table 5. The δ phase is more stable at lower temperature when compared to the Laves phase. This was observed in the Thermo-Calc predictions, Fig. 1. Furthermore, the microstructures shown in Fig. 5(a-c) clearly indicate an increased stability of the δ phase with increasing Nb and decreasing Al associated with the gradual absence of the secondary Laves. Studies on phase formation in the Ni-Cr-Fe-Nb system show that a three phase field exists between γ, δ and C14-Laves [30], hence the reduced Al content would tend to stabilize the δ precipitates over the γ′. In addition, when the Nb-rich δ precipitates form, this serves to deplete the system of Nb and

435 decreases the likelihood for the precipitation of the secondary Laves. Heat treatment above the δ
436 solvus temperature, at 1000°C for alloy 9Fe-4Al-8Nb, resulted in the preferential formation of
437 secondary Laves, Fig. 6(c), that were not observed at lower temperatures, over the precipitation
438 of the δ phase. Doubling the Fe content further increased the stability of the secondary Laves as
439 Fe preferentially partitions to the Laves phase and less Ni is available for δ precipitation.
440 Additionally, the δ phase solvus temperature decreased, Fig. 2. Therefore, in the 18 at.% Fe
441 alloys, a greater amount of secondary Laves were formed and δ phase was only observed in alloy
442 18Fe-4Al-8Nb after heat treatment at 800°C, Fig. 4(f).

443 A second precipitation dependence was noted with respect to the γ′ and NiAl phases. The
444 NiAl phase was only observed in the 18 at.% Fe alloys even though the increased addition of Fe
445 resulted in a lower overall Ni content (22 at.% Ni) compared to the 9 at.% Fe alloys (31 at.% Ni).
446 Therefore, the precipitation of the NiAl phase can likely be attributed to two factors. First, TEM-
447 EDS analysis revealed partitioning of Fe to NiAl, Table 5. Therefore, Fe additions were found to
448 promote the formation of NiAl by stabilizing the phase and increasing its solvus temperature,
449 Fig. 2. In addition, the $Ni_3Fe$ phase possesses a relatively low solvus temperature [31], hence any
450 substitution of Fe into the $Ni_3$(Al, Nb) would likely decrease the phase stability in comparison to
451 NiAl. Second, with the reduced availability of Ni in solution for the 18 at.% Fe alloys, γ′
452 precipitation was unfavorable resulting in Ni and Al solute atoms being available for the
453 formation of NiAl. Thus, γ′ formation becomes more favorable in the 9 at.% Fe alloys while
454 NiAl precipitation is promoted in the 18 at.% Fe alloys. Furthermore, as the Laves phase has
455 limited solubility for Al, interfacial segregation of Al atoms associated with the growth of Laves
456 phase, creates Al rich zones along the Laves/γ interface, subsequently contributing to the
457 formation of NiAl, Fig. 5(d,e). Various studies have reported that the occurrence of the NiAl
458 phase can be significantly detrimental to the high-temperature mechanical properties or
459 machinability of alloys, particularly when present at the interface of other secondary phases [41].

460

461 **4.4. Thermodynamic predictions**

462 Thermo-Calc predictions were performed using both the TCNi8 and TTNi8 databases for
463 comparison. The Laves and NiAl phase compositions were compared to the TEM-EDS results
464 for TCNi8 and TTNi8 in Fig. 11. In the Laves phase, Fig. 11(a), TCNi8 reported Co, Cr, Fe and
465 Nb contents close to those measured on the TEM as well as partitioning of Al. Although phase

stability predictions from TTNi8 were in relatively good agreement, the predicted phase chemistries were not in close agreement with the experimental data. More significant differences were observed in the NiAl phase, Fig. 11(b). Comparing the phase chemistry predictions from the two databases, it appears that TCNi8 shows better agreement with the TEM-EDS results when compared to TTNi8, particularly with respect to Al, Co, Cr, Fe and Nb levels. Interestingly, TTNi8 more accurately described the stability of the primary Laves showing stable Laves phase up to the incipient melting temperature for all alloys but 9Fe-8Al-4Nb. However, both databases were not able to capture the differences between the primary and secondary Laves, as the latter was observed to dissolve prior to reaching the incipient melting temperature. Overall, phase formation and stability were better predicted using the TTNi8 database, which showed γ′ precipitation if η was removed and more accurate NiAl predictions. This is likely due to the predicted composition of the η phase $(Ni,Co)_6AlNb$ with major partitioning of elements constituting of the γ' phase. It should be noted, however, that it is likely possible that η phase would precipitate in this set of alloys, however, this would likely happen after a prolonged exposure time at temperature and is beyond the scope of this investigation. Such a phase is known to show intergrowth with the δ phase [42,43], however, no extra diffraction spots or minor peaks were observed in the TEM-SAD patterns or XRD patterns, respectively. It should be noted that the solvus temperature predictions for the various precipitate phases lack in accuracy, which is most likely due to the complex microstructures formed in this set of alloys.

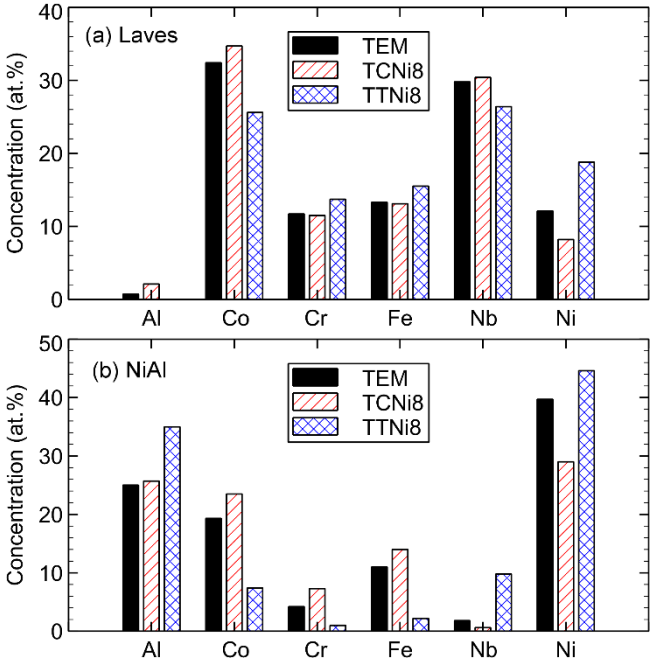


**Fig. 11.** Elemental concentrations of (a) the Laves and (b) NiAl phases from the TEM measurements and from Thermo-Calc using the TCNi8 and TTNi8 databases under similar conditions.

### 4.5. Outlook

Finally, Liu et al. studied microstructures in the NiCoCrFe system with varying Nb additions and, although no γ′ phase was observed, excessive alloying with Nb resulted in the formation of a C14-Laves phase $(CoCrFeNi)_2(CrNb)$ [28]. Even though these alloys have a relatively high entropy of mixing, the individual enthalpy of each constituent cannot be ignored. Nb has a large enthalpy of mixing with the other elements, which promotes intermetallic phase formation. From a precipitation-strengthened alloy design view, this effect can be exploited to promote the formation of select secondary phases. Although the Laves phase is a high-entropy intermetallic phase [44], it brings in a considerable drop of ductility in the NiCoCrFe system, due to crack formation in the Nb-rich Laves regions [28]. The synergistic effect of Nb and Al to promote stable γ′ formation could be utilized in designing two phase alloys for high temperature applications where adequate creep resistance is needed. Similarly, Ti and Al additions can promote the formation of stable γ′ phase precipitates, however, excessive amounts result in the formation of a $L2_1$ Heusler type phase [20,21]. Locating desirable compositions requires further

505 exploration of the Ni-Co-Cr-Fe system with additions of elements that have high individual
506 enthalpies of formation and that show synergistic effects with one another.
507

508 **5. Conclusions**

509 Based on the results and observations presented in this study, the following conclusions can be
510 reported:

511 1. Primary C14-Laves phase is stable up to the incipient melting temperature in the HEAs
512 with 9 at.% Fe when the Nb concentration is greater than or equal to 6 at.% and in the
513 HEAs with 18 at.% Fe. Both Fe and Nb stabilize the primary C14-Laves phase with Nb
514 being a stronger stabilizer on a per at.% basis, likely due to the higher individual enthalpy
515 of mixing.
516 2. Secondary C14-Laves formed at or above 900°C in the 9 at.% Fe alloys and 800°C in the
517 18 at.% alloys in the form of sub-micron sized plates. A higher number density was
518 found in the HEAs containing 18 at.% Fe. Although Nb is one of the major constituent
519 elements, the number density of the secondary Laves decreased with increasing Nb
520 content from the higher fraction of primary Laves present after homogenization. The
521 secondary Laves precipitates dissolved after heat treatment at 1100°C for 100 h in the
522 alloys containing primary Laves.
523 3. The δ phase is more stable than the secondary Laves as its presence in the microstructure
524 of the alloys prevented the formation of the sub-micron sized Laves plates. Dissolution of
525 the δ phase following heat treatment above its solvus temperature resulted in the
526 precipitation of the secondary Laves from the Nb back into solution. Fe is a stronger
527 Laves stabilizer than δ stabilizer. The morphology of the δ phase was of Widmanstätten
528 type, forming a net structure within the matrix and larger thin plates at the primary
529 Laves/γ interface.
530 4. Fe was found to partition to the NiAl phase. Higher Fe concentrations resulted in the
531 stability of NiAl instead of γ′ precipitates. γ′ precipitation was possible in the alloys with
532 9 at.% Fe and higher Al content, showing the synergistic effect of Al and Nb on γ′ phase
533 formation.
534 5. Overall, TCNi8 was more accurate at predicting phase compositions while TTNi8
535 showed better phase formation/stability predictions.

## Acknowledgments

This technical effort was performed, in part, in support of the National Energy Technology Laboratory's ongoing research in advanced alloy development under the RES contract DE-FE0004000. Financial support for the work performed at USTB was provided under the grant number FRF-TP-17-085A1.

## Disclaimer

This project was funded, in part, by the Department of Energy, National Energy Technology Laboratory, an agency of the United States Government, through a support contract with AECOM. Neither the United States Government nor any agency thereof, nor any of their employees, nor AECOM, nor any of their employees, makes any warranty, expressed or implied, or assumes any legal liability or responsibility for the accuracy, completeness, or usefulness of any information, apparatus, product, or process disclosed, or represents that its use would not infringe privately owned rights. Reference herein to any specific commercial product, process, or service by trade name, trademark, manufacturer, or otherwise, does not necessarily constitute or imply its endorsement, recommendation, or favoring by the United States Government or any agency thereof. The views and opinions of authors expressed herein do not necessarily state or reflect those of the United States Government or any agency thereof.

## References

[1] T.P. Gabb, R.A. MacKay, S.L. Draper, C.K. Sudbrack, M. V Nathal, The mechanical properties of candidate superalloys for a hybrid turbine disk, Cleveland, Ohio, 2013. https://ntrs.nasa.gov/archive/nasa/casi.ntrs.nasa.gov/20140000732.pdf.

[2] J. Sato, T. Omori, K. Oikawa, I. Ohnuma, R. Kainuma, K. Ishida, Cobalt-Base High-Temperature Alloys, Science (80-. ). 312 (2006) 90–91. doi:10.1126/science.1121738.

[3] C.T. Sims, N.S. Stoloff, W.C. Hagel, Superalloys II: High-Temperature Materials for Aerospace and Industrial Power, John Wiley & Sons Inc, Hoboken, NJ, 1987.

[4] R.C. Reed, The Superalloys: Fundamentals and Applications, Cambridge University Press, New York, 2006. doi:10.1017/CBO9780511541285.

[5] A. Mottura, A. Janotti, T.M. Pollock, A first-principles study of the effect of Ta on the superlattice intrinsic stacking fault energy of L12-Co3(Al,W), Intermetallics. 28 (2012) 138–143. doi:10.1016/j.intermet.2012.04.020.

[6] K.V. Vamsi, S. Karthikeyan, Modelling ternary effects on antiphase boundary energy of Ni3Al, MATEC Web Conf. 14 (2014) 11005. doi:10.1051/matecconf/20141411005.

[7] Y. Mishima, S. Ochiai, N. Hamao, M. Yodogawa, T. Suzuki, Solid Solution Hardening of Ni3Al with Ternary Additions, Trans. Japan Inst. Met. 27 (1986) 648–655. doi:10.2320/matertrans1960.27.648.

[8] Y. Mishima, S. Ochiai, M. Yodogawa, T. Suzuki, Mechanical Properties of Ni3Al with Ternary Addition of Transition Metal Elements, Trans. Japan Inst. Met. 27 (1986) 41–50. doi:10.2320/matertrans1960.27.41.

[9] T.M. Pollock, R.D. Field, Chapter 63 Dislocations and high-temperature plastic deformation of superalloy single crystals, Dislocations in Solids. 11 (2002) 547–618. doi:10.1016/S1572-4859(02)80014-6.

[10] A.K. Jena, M.C. Chaturvedi, The role of alloying elements in the design of nickel-base superalloys, J. Mater. Sci. 19 (1984) 3121–3139. doi:10.1007/BF00549796.

[11] G.W. Meetham, Trace elements in superalloys–an overview, Met. Technol. 11 (1984) 414–418. doi:10.1179/030716984803275188.

[12] B.C. Yan, J. Zhang, L.H. Lou, Effect of boron additions on the microstructure and transverse properties of a directionally solidified superalloy, Mater. Sci. Eng. A. 474 (2008) 39–47. doi:10.1016/j.msea.2007.05.082.

[13] T.J. Garosshen, T.D. Tillman, G.P. Mccarthy, Effects of B, C, and Zr on the Structure and Properties of a P/M Nickel Base Superalloy, Metall. Trans. A. 18A (1987) 69–77. doi:10.1007/BF02646223.

[14] P. Kontis, E. Alabort, D. Barba, D.M. Collins, A.J. Wilkinson, R.C. Reed, On the role of boron on improving ductility in a new polycrystalline superalloy, Acta Mater. 124 (2017) 489–500. doi:10.1016/j.actamat.2016.11.009.

[15] P. Kontis, H.A.M. Yusof, S. Pedrazzini, M. Danaie, K.L. Moore, P.A.J. Bagot, M.P. Moody, C.R.M. Grovenor, R.C. Reed, On the effect of boron on grain boundary character in a new polycrystalline superalloy, Acta Mater. 103 (2016) 688–699. doi:10.1016/j.actamat.2015.10.006.

[16] T.-K. Tsao, A.-C. Yeh, C.-M. Kuo, K. Kakehi, H. Murakami, J.-W. Yeh, S.-R. Jian, The High Temperature Tensile and Creep Behaviors of High Entropy Superalloy, Sci. Rep. 7 (2017) 12658. doi:10.1038/s41598-017-13026-7.

[17] W. Zhang, P.K. Liaw, Y. Zhang, Science and technology in high-entropy alloys, Sci. China Mater. 61 (2018) 2–22. doi:10.1007/s40843-017-9195-8.

[18] Y. Zhang, T.T. Zuo, Z. Tang, M.C. Gao, K.A. Dahmen, P.K. Liaw, Z.P. Lu, Microstructures and properties of high-entropy alloys, Prog. Mater. Sci. 61 (2014) 1–93. doi:10.1016/j.pmatsci.2013.10.001.

[19] B.F. Dyson, M. McLean, Creep deformation of evgineering alloys: Developments from physical modelling., ISIJ Int. 30 (1990) 802–811. doi:10.2355/isijinternational.30.802.

[20] J.Y. He, H. Wang, H.L. Huang, X.D. Xu, M.W. Chen, Y. Wu, X.J. Liu, T.G. Nieh, K. An, Z.P. Lu, A precipitation-hardened high-entropy alloy with outstanding tensile properties, Acta Mater. 102 (2016) 187–196. doi:10.1016/j.actamat.2015.08.076.

[21] J.Y. He, H. Wang, Y. Wu, X.J. Liu, H.H. Mao, T.G. Nieh, Z.P. Lu, Precipitation behavior and its effects on tensile properties of FeCoNiCr high-entropy alloys, Intermetallics. 79 (2016) 41–52. doi:10.1016/j.intermet.2016.09.005.

[22] E.J. Pickering, R. Muñoz-Moreno, H.J. Stone, N.G. Jones, Precipitation in the equiatomic high-entropy alloy CrMnFeCoNi, Scr. Mater. 113 (2016) 106–109. doi:10.1016/j.scriptamat.2015.10.025.

[23] S. Guo, C. Ng, J. Lu, C.T. Liu, Effect of valence electron concentration on stability of fcc or bcc phase in high entropy alloys, J. Appl. Phys. 109 (2011) 103505. doi:10.1063/1.3587228.

[24] H.M. Daoud, A. Manzoni, R. Völkl, N. Wanderka, U. Glatzel, Microstructure and Tensile Behavior of Al8Co17Cr17Cu8Fe17Ni33 (at.%) High-Entropy Alloy, JOM. 65 (2013) 1805–1814. doi:10.1007/s11837-013-0756-3.

[25] E.J. Pickering, H.J. Stone, N.G. Jones, Fine-scale precipitation in the high-entropy alloy Al0.5CrFeCoNiCu, Mater. Sci. Eng. A. 645 (2015) 65–71. doi:10.1016/j.msea.2015.08.010.

[26] H.M. Daoud, A.M. Manzoni, R. Völkl, N. Wanderka, U. Glatzel, Oxidation Behavior of Al8Co17Cr17Cu8Fe17Ni33, Al23Co15Cr23Cu8Fe15Ni15, and Al17Co17Cr17Cu17Fe17Ni17 Compositionally Complex Alloys (High-Entropy Alloys) at Elevated Temperatures in Air, Adv. Eng. Mater. 17 (2015) 1134–1141. doi:10.1002/adem.201500179.

[27] H.M. Daoud, A.M. Manzoni, N. Wanderka, U. Glatzel, High-Temperature Tensile Strength of Al10Co25Cr8Fe15Ni36Ti6 Compositionally Complex Alloy (High-Entropy Alloy), JOM. 67 (2015) 2271–2277. doi:10.1007/s11837-015-1484-7.

[28] W.H. Liu, J.Y. He, H.L. Huang, H. Wang, Z.P. Lu, C.T. Liu, Effects of Nb additions on the microstructure and mechanical property of CoCrFeNi high-entropy alloys, Intermetallics. 60 (2015) 1–8. doi:10.1016/j.intermet.2015.01.004.

[29] S.G. Ma, Y. Zhang, Effect of Nb addition on the microstructure and properties of AlCoCrFeNi high-entropy alloy, Mater. Sci. Eng. A. 532 (2012) 480–486. doi:10.1016/j.msea.2011.10.110.

[30] M. Takeyama, S. Morita, A. Yamauchi, M. Yamanaka, T. Matsuo, Phase Equilibria Among γ, Ni3Nb-δ and Fe2Nb-ε Phases in Ni-Nb-Fe and Ni-Nb-Fe-Cr Systems at Elevated Temperatures, in: Superalloys 718, 625, 706 Var. Deriv., TMS, 2001: pp. 333–344. doi:10.7449/2001/Superalloys_2001_333_344.

[31] D. Connétable, M. Mathon, J. Lacaze, First principle energies of binary and ternary phases of the Fe–Nb–Ni–Cr system, Calphad. 35 (2011) 588–593. doi:10.1016/j.calphad.2011.09.004.

[32] S. Antonov, M. Detrois, S. Tin, Design of Novel Precipitate-Strengthened Al-Co-Cr-Fe-Nb-Ni High-Entropy Superalloys, Metall. Mater. Trans. A. 49 (2018) 305–320. doi:10.1007/s11661-017-4399-9.

[33] S. Antonov, M. Detrois, D. Isheim, D. Seidman, R.C. Helmink, R.L. Goetz, E. Sun, S. Tin, Comparison of thermodynamic database models and APT data for strength modeling in high Nb content γ-γ' Ni-base superalloys, Mater. Des. 86 (2015) 649–655. doi:10.1016/j.matdes.2015.07.171.

[34] C.A. Schneider, W.S. Rasband, K.W. Eliceiri, NIH Image to ImageJ: 25 years of image analysis, Nat. Methods. 9 (2012) 671–675. doi:10.1038/nmeth.2089.

[35] S. Antonov, M. Detrois, Automation of γ′ precipitate and other particle quantification and calculation of inter-particle spacing using an ImageJ script, Micron. (n.d.).

[36] B.H. Toby, R.B. Von Dreele, GSAS-II : the genesis of a modern open-source all purpose

crystallography software package, J. Appl. Crystallogr. 46 (2013) 544–549. doi:10.1107/S0021889813003531.

[37] K. Momma, F. Izumi, VESTA 3 for three-dimensional visualization of crystal, volumetric and morphology data, J. Appl. Crystallogr. 44 (2011) 1272–1276. doi:10.1107/S0021889811038970.

[38] S. Guo, C.T. Liu, Phase stability in high entropy alloys: Formation of solid-solution phase or amorphous phase, Prog. Nat. Sci. Mater. Int. 21 (2011) 433–446. doi:10.1016/S1002-0071(12)60080-X.

[39] C. Zhang, F. Zhang, H. Diao, M.C. Gao, Z. Tang, J.D. Poplawsky, P.K. Liaw, Understanding phase stability of Al-Co-Cr-Fe-Ni high entropy alloys, Mater. Des. 109 (2016) 425–433. doi:10.1016/j.matdes.2016.07.073.

[40] P.D. Jablonski, J.A. Hawk, Homogenizing Advanced Alloys: Thermodynamic and Kinetic Simulations Followed by Experimental Results, J. Mater. Eng. Perform. 26 (2017) 4–13. doi:10.1007/s11665-016-2451-3.

[41] M. Detrois, P.D. Jablonski, Formation of β-NiAl Phase During Casting of a Ni-Based Superalloy, Metall. Mater. Trans. B. 49 (2018) 524–528. doi:10.1007/s11663-018-1202-2.

[42] S. Antonov, M. Detrois, R.C. Helmink, S. Tin, Precipitate phase stability and compositional dependence on alloying additions in γ-γ′-δ-η Ni-base superalloys, J. Alloys Compd. 626 (2015) 76–86. doi:10.1016/j.jallcom.2014.11.155.

[43] E.J. Pickering, H. Mathur, A. Bhowmik, O.M.D.M. Messé, J.S. Barnard, M.C. Hardy, R. Krakow, K. Loehnert, H.J. Stone, C.M.F. Rae, Grain-boundary precipitation in Allvac 718Plus, Acta Mater. 60 (2012) 2757–2769. doi:10.1016/j.actamat.2012.01.042.

[44] M.-H. Tsai, Three Strategies for the Design of Advanced High-Entropy Alloys, Entropy. 18 (2016) 252. doi:10.3390/e18070252.